ADVANCED FUNCTIONAL MATERIALS
www.afm-journal.de

A Composite Strategy on $H_2V_3O_8$ and Carbon Fibers: Boosting the Mechanical and Electrochemical Performance of the Fiber Cathodes in Zinc-Ion Fiber Batteries

Jiayi Xu, Zhen Zhu, Linfeng Hu, Jing Wang, Jingsong Liu, Kang Yan, and Kongjun Zhu**

Flexible fiber batteries can be integrated into irregular spaces, allowing conventional structures to store energy. Preserving electrochemical performance while improving mechanical strength can substantially broaden their application potential. Here, $H_2V_3O_8$ and nickel-plated carbon fibers are combined for the first time to construct a composite fiber cathode for zinc-ion fiber batteries. A continuous wet spinning and pressing method is employed to fabricate the fiber cathode, leveraging the respective advantages of the core and active materials. The nickel-plated carbon fibers, which exhibit high electrical conductivity, serve effectively as current collectors, and their favorable mechanical properties confer excellent flexibility and an ultimate tensile strength of 361.9 MPa to the fiber electrode. Owing to the deformability of carbon fibers and the pressing step, the electrode acquires a rectangular cross-section, which contributes to improved electrochemical performance. When assembled with a zinc/carbon fibers composite anode and a hydrogel electrolyte into a battery, it delivers a specific capacity of 138 mAh g^{-1} at 3 A g^{-1} after 1500 cycles. This work demonstrates a balance between mechanical and electrochemical performance in fiber electrodes, supporting their potential for structural energy storage applications.

1. Introduction

In recent years, 1D fiber batteries have attracted considerable research interest due to their flexibility, which enables application in textile batteries and flexible electronic devices.[1] Their shape adaptability allows deployment in irregular spaces, improving volumetric utilization in various structures and providing energy storage capacity. This broadens the application prospects of fiber batteries and places higher demands on energy storage capacity, strength, and safety. Zinc-ion batteries feature low cost, high theoretical capacity, and good safety, making them a competitive option for fiber batteries.[2–4] Fiber electrodes are a fundamental component of fiber batteries, and their improvement can directly enhance both electrochemical and mechanical performance.

Improvements in the electrochemical performance of fiber electrodes primarily rely on optimization of the active materials. Vanadium materials have received much attention because of their multivalency, low cost, large layer spacing, and high theoretical capacity.[5] Among them, $H_2V_3O_8$ possesses structural features that confer specific advantages for zinc-ion batteries. $H_2V_3O_8$ consists of stacked V_3O_8 layers connected by hydrogen bonds, with each layer comprising VO_6 octahedra and VO_5 trigonal bipyramids.[6] The large interlayer spacing favors intercalation of Zn^{2+}, while the hydrogen bonds between V_3O_8 layers stabilize the structure during charge/discharge, enabling long-term cycling stability.[7,8] Therefore, $H_2V_3O_8$ is a promising active material for high-performance zinc-ion fiber batteries.

Achieving both high energy storage capacity and mechanical strength in fiber electrodes requires research into their structural design. Fiber electrodes without cores rely only on polymeric bonding and support, resulting in lower tensile strength. Core–sheath fiber electrodes offer greater advantages, with active materials built on a core such as metal wires,[9,10] polymer fibers,[11,12] or carbon nanotube fibers.[13] However, the core material is typically utilized only as a substrate to maintain structure during fabrication, which has led to a lack of further research on cores. Carbon fiber (CF) is a favorable core material because it is lighter and more flexible than metal wires, exhibits higher tensile strength than polymer fibers, and is less expensive than carbon nanotube fibers. However, the high resistance of CF limits its use in fiber electrodes. In previous work using CF as the core, the active materials were often modified to improve the overall electrical conductivity of electrode,[14,15] but this also complicated

J. Xu, Z. Zhu, J. Wang, K. Yan, K. Zhu
State Key Laboratory of Mechanics and Control for Aerospace Structures
College of Aerospace Engineering
Nanjing University of Aeronautics and Astronautics
Nanjing 210016, P. R. China
E-mail: kjzhu@nuaa.edu.cn

L. Hu
School of Materials Science and Engineering
Southeast University
Nanjing 211189, P. R. China
E-mail: linfenghu@seu.edu.cn

J. Liu
College of Materials Science and Technology
Nanjing University of Aeronautics and Astronautics
Nanjing 210016, P. R. China

The ORCID identification number(s) for the author(s) of this article can be found under https://doi.org/10.1002/adfm.202510244

DOI: 10.1002/adfm.202510244

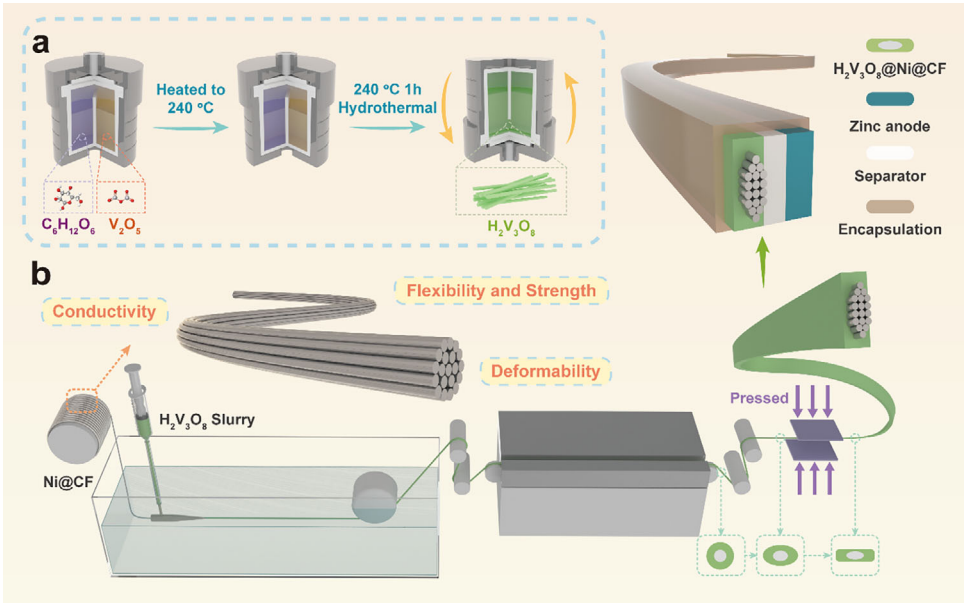

Figure 1. Schematic of the setup. a) Synthesis process for $H_2V_3O_8$ nanowires. b) Preparation process for the $H_2V_3O_8$@Ni@CF//Zn fiber batteries.

the fabrication process. Therefore, direct optimization of CF can offer greater applicability and convenience.

Unfortunately, no efficient method has been developed for forming a composite of $H_2V_3O_8$ and CF. Among common composite strategies,[16–20] the coating method suffers from low slurry utilization, and electrodeposition is not suitable for vanadium oxides. Given the limited active sites on the CF surface, direct growth of $H_2V_3O_8$ on it also shows much difficulty. Hence, it is challenging to develop a universal method for fabricating fiber electrodes with composite structures, which can exert the electrochemical asdvantage of active materials and the mechanical superiority of CF simultaneously.

Herein, a high-performance $H_2V_3O_8$/CF composite cathode for zinc-ion fiber batteries was developed. High-purity $H_2V_3O_8$ powder was synthesized by a simple one-step high-temperature hydrothermal method. Instead of traditional CF, the nickel-plated carbon fiber (Ni@CF) was used as the core, providing improved conductivity as a current collector. $H_2V_3O_8$ was then adhered to the Ni@CF by core-containing extrusion. Benefiting from the deformability of CF, the fiber electrodes were pulled and pressed into a rectangular cross-section before assembly, unlike conventional electrodes with circular cross-sections. The wet spinning and pressing method provided a more compact structure and improved the electric field distribution near the electrodes, which was suitable for fiber batteries with a parallel electrode arrangement. The composite fiber cathode achieved an ultimate tensile strength of 361.9 MPa. When assembled into a fiber battery with a zinc strip as the counter electrode, the fiber cathode demonstrated a specific capacity of 225 mAh g^{-1} at a current density of 3 A g^{-1}. To ensure overall flexibility, a zinc/CF composite electrode was used as the negative electrode, and a polyacrylamide (PAM) hydrogel was employed as the electrolyte. This configuration enabled efficient cycling performance for 1500 cycles, delivering 138 mAh g^{-1} at 3 A g^{-1}. These results indicate that the fabricated fiber electrodes possess favorable electrochemical and mechanical performance.

2. Results and Discussion

2.1. Morphological Characterization of the $H_2V_3O_8$ Nanowires

Figure 1a illustrates the one-step hydrothermal synthesis of $H_2V_3O_8$ using a high-temperature mixed method. Detailed preparation procedures are provided in the experimental section. This synthetic strategy avoids the formation of intermediate phases and defects that commonly occur during traditional hydrothermal heating ramp-up. Therefore, reaction time is reduced, and the crystallinity of the samples is significantly enhanced.[21] Therefore, large quantities of powder can be synthesized efficiently, supporting subsequent large-scale fiber preparation.

The microstructure of the $H_2V_3O_8$ powder was analyzed by scanning electron microscopy (SEM). As shown in **Figure** 2a, the sample consisted of ultrathin nanowires. X-ray diffraction (XRD) was performed to analyze the crystal structure. As shown in Figure 2b, all diffraction peaks were indexed to the standard powder diffraction file (PDF) card for orthorhombic $H_2V_3O_8$ (No. 85–2401), confirming excellent crystallinity. Raman spectrum (Figure 2c) further confirmed the structure. The principal peaks below 1200 cm^{-1} at 125, 267, 390, 512, 675, 862, and 980 cm^{-1} were assigned to $H_2V_3O_8$.[22] The peaks at 267 and 390 cm^{-1} corresponded to the bending vibrations of V—O, while those at 512, 675, and 862 cm^{-1} were attributed to the stretching vibrations of V—O. The strong peak at 980 cm^{-1} originated from the terminal oxygen (V═O) stretching vibration. The peak at 125 cm^{-1} was ascribed to the stretching mode of $(V_2O_2)_n$, reflecting the chain translation.[23] X-ray photoelectron spectroscopy (XPS) was used to analyze chemical composition and elemental valence states. The survey spectrum (Figure 2d) indicated the presence of only

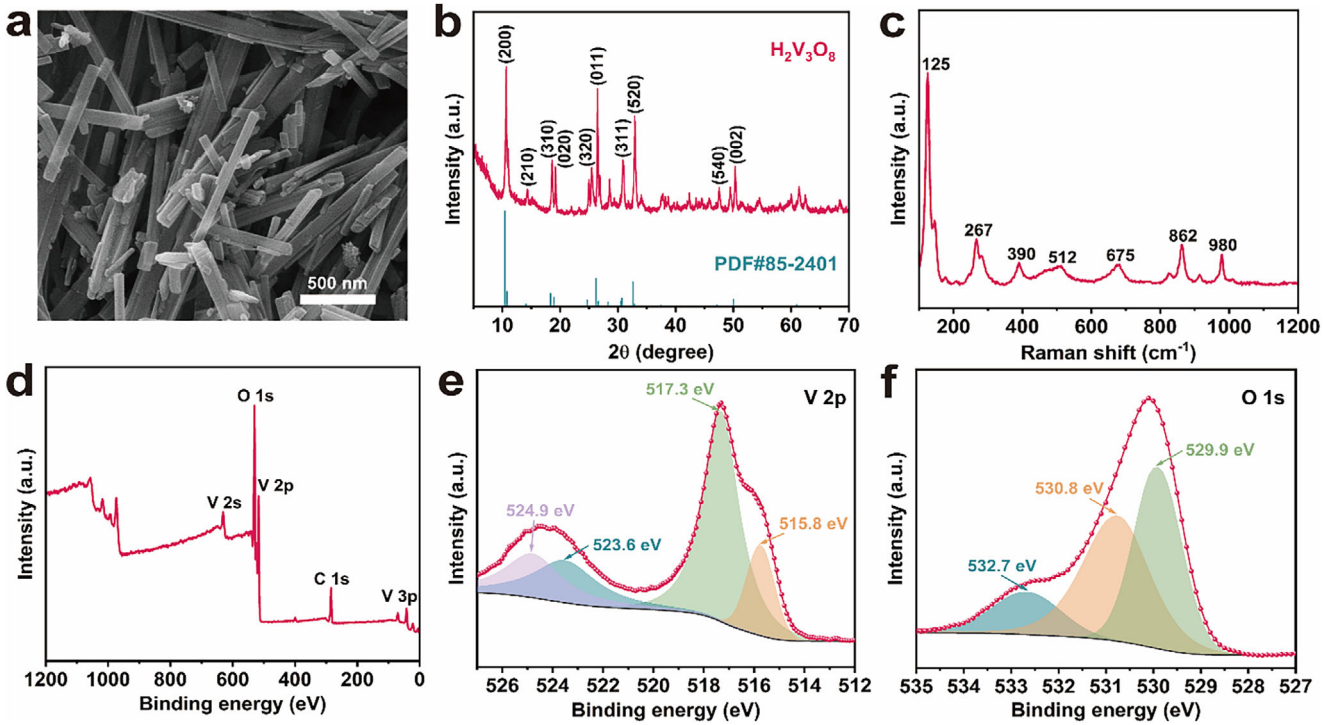

Figure 2. Structural characterization of the $H_2V_3O_8$ powder. a) SEM image. b) XRD patterns. c) Raman spectrum. d) XPS spectrum. e,f) High-resolution XPS spectra of V and O.

V, O, and C. Figure 2e presents the high-resolution V 2p XPS spectrum, where peaks at 515.8 and 517.3 eV corresponded to V $2p_{3/2}$, and those at 523.6 and 524.9 eV corresponded to V $2p_{1/2}$. Peaks at 515.8 and 523.6 eV were assigned to V^{4+}, and those at 517.3 eV and 524.9 eV to V^{5+}. The V 2p spectrum confirmed the coexistence of V^{4+} and V^{5+}, consistent with the XRD results. The high-resolution O 1s spectrum (Figure 2f) displayed peaks at 529.9, 530.8, and 532.7 eV, attributed to O—V^{5+}, HO—V, and O—V^{4+} bonds, respectively.

2.2. Design and Realization of the Composite Fiber Cathode

Given that fiber batteries may be subjected to tensile loading in practical applications, a core–sheath structure was designed for the fiber electrodes. The core enhanced mechanical properties and served as the current collector, requiring both high mechanical strength and electrical conductivity. CF was selected for its excellent tensile strength. However, conventional CF exhibited high resistance, making it unsuitable as a current collector in the fiber electrode. The high resistance was attributed to the surface sizing agent, and this did not improve after acetone treatment. Therefore, Ni@CF was utilized in this study (Figure S1, Supporting Information). The 1k Ni@CF achieved a line resistance of 0.25 Ω cm^{-1}, a significant reduction compared to untreated 1k CF (7.50 Ω cm^{-1}) and acetone-treated 1k CF (6.07 Ω cm^{-1}) (Figure S2, Supporting Information).

The structure of the fiber electrode and the design of its fabrication process are closely linked. It is challenging to synthesize $H_2V_3O_8$ directly on CF due to the lack of active sites on its surface. The wet spinning method offers a simple and efficient process suitable for large-scale fiber production. This study employed a special nozzle with coaxial dual channels (Figure S3, Supporting Information) to continuously prepare the composite fiber electrode. The fabrication process is illustrated in Figure 1b. The special tapered concave nozzle allowed the slurry to adhere effectively to the core. This method imposes no limitation on the choice of active and core materials, enabling a successful combination of $H_2V_3O_8$ and Ni@CF.

The fiber cathodes were flexible and could be knotted, bear heavy loads, and be wrapped (**Figure** 3a–d). The SEM image (Figure 3e) showed the surface morphology of the $H_2V_3O_8$ fiber electrode with the Ni@CF core ($H_2V_3O_8$@Ni@CF), revealing good uniformity. The magnified image (Figure S4, Supporting Information) displayed $H_2V_3O_8$ nanowires within the fiber electrode, matching those in Figure 2a. Energy-dispersive X-ray (EDX) mappings (Figure 3f–h) confirmed the uniform distribution of the electrode materials on the fiber surface, where V indicated the active material ($H_2V_3O_8$) and F indicated the binder (polyvinylidene fluoride, PVDF). Ni, which indicated Ni@CF, was hardly observed, illustrating that the coating effectively enveloped the core.

2.3. Structural Optimization of the Fiber Cathodes

The cross-sectional SEM image and EDX mappings (**Figure** 4a–c) clearly demonstrated the structure of $H_2V_3O_8$@Ni@CF. The active material coating tightly adhered to the Ni@CF core. The cross-sectional shape of fiber

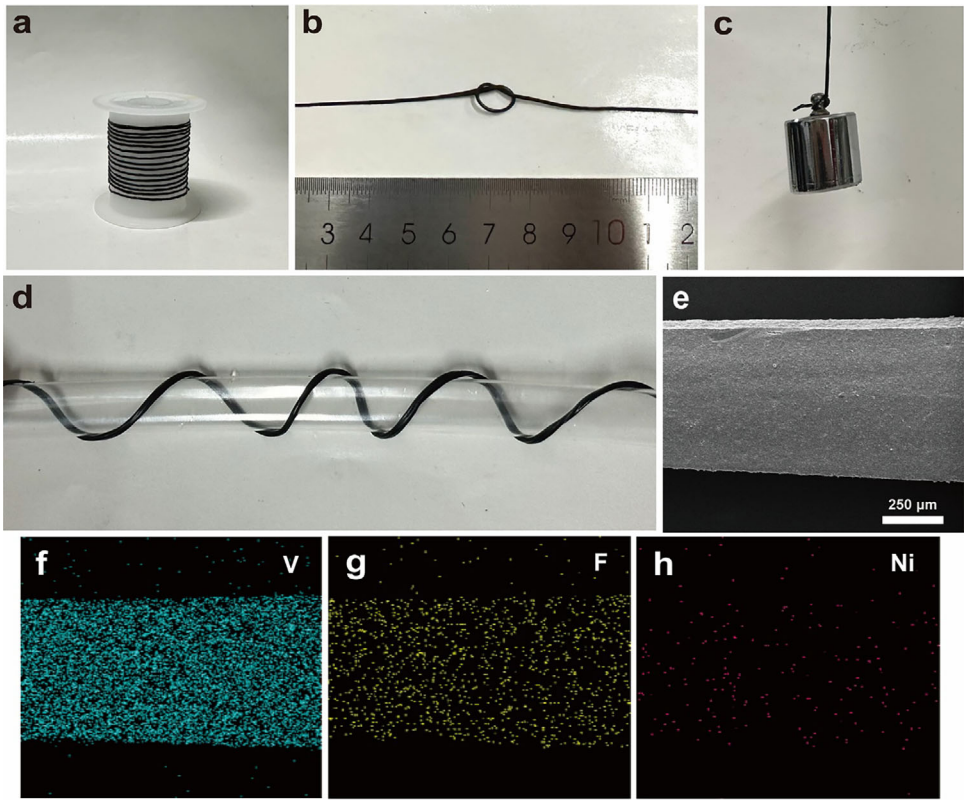

Figure 3. Photographs and structural characterization of $H_2V_3O_8$@Ni@CF. a) A reel of $H_2V_3O_8$@Ni@CF. b–d) Flexibility and load-bearing capability: b) knotting, c) weight loading, and d) wrapping. e) Surface SEM image of $H_2V_3O_8$@Ni@CF. f–h) EDX mappings of $H_2V_3O_8$@Ni@CF.

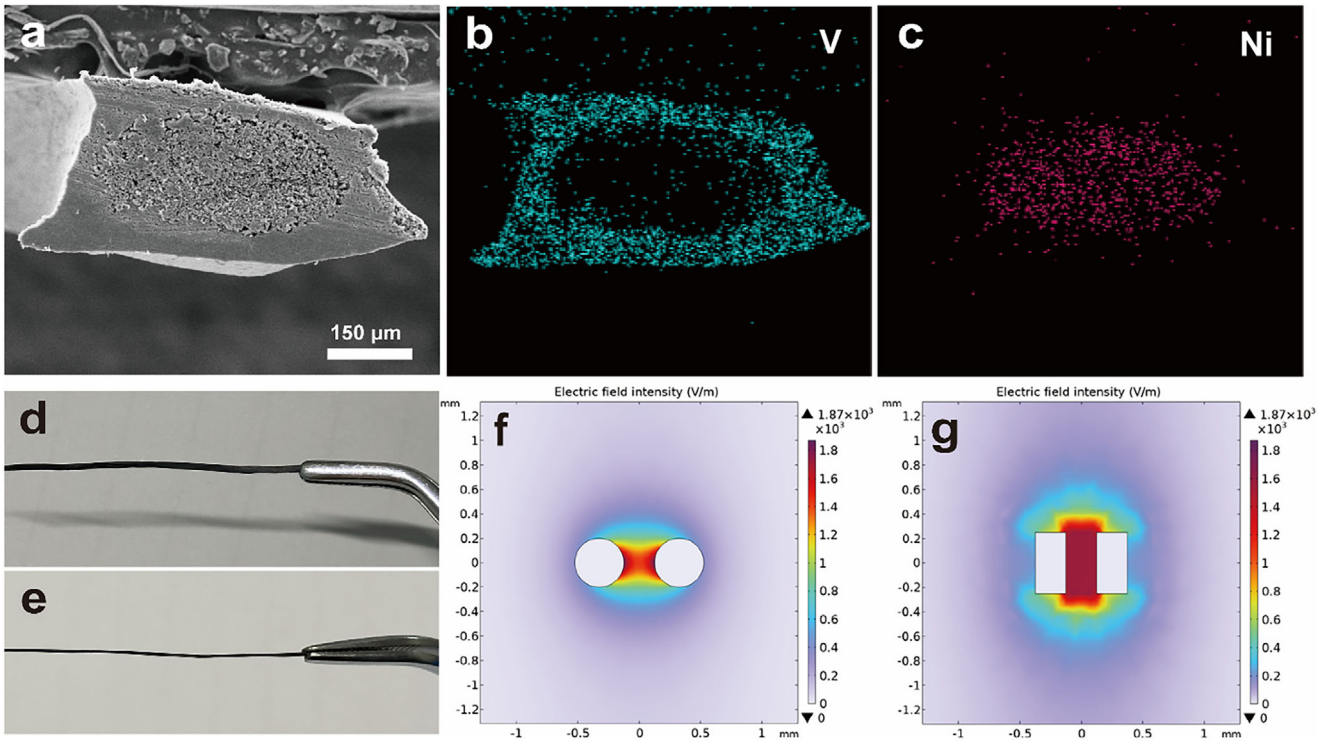

Figure 4. Analysis of the cross-section of $H_2V_3O_8$@Ni@CF. a) SEM image of the cross-section. b,c) EDX mappings of the cross-section. d,e) Photographs of $H_2V_3O_8$@Ni@CF from front and side views. f,g) Electric field intensity simulations of fiber batteries with circular and rectangular electrodes.

electrodes is typically circular, determined by the existing preparation process and the core material selection. For core–sheath fiber electrodes, the metallic or polymeric fiber cores usually have a circular cross-section. When active materials are coated or grown on these cores, the resulting electrodes also exhibit a circular cross-section. For fiber electrodes without cores, which are fabricated by extrusion or 3D printing, their cross-sections also tend to be circular because round nozzles are used to reduce friction and maintain flow stability during extrusion. Therefore, fiber electrodes with a circular cross-section are common. It is generally challenging to alter the cross-sectional shape due to the resistance to deformation along the radial direction in metallic wires and polymeric fibers. Notably, Khudiyev et al. fabricated fiber batteries with a rectangular cross-section by employing a special thermal stretching technique and cuboid raw materials.[24]

In contrast to rigid metallic or twisted polymeric fibers, CF provides satisfactory shape deformability. The Ni@CF core used here consists of 1000 parallel CF filaments. Therefore, the fiber electrode could be mechanically pulled and pressed to transform its cross-sectional shape from circular (Figure S5, Supporting Information) to rectangular (Figure 4a,d,e). Pressing the electrode densified the active material. In addition, when both cathode and anode adopt a parallel arrangement, the rectangular fiber electrodes conferred electrochemical advantages over circular ones. A brief explanation follows. Ion transport in the electrolyte occurs primarily through diffusion and migration, as convection can be neglected under typical battery conditions without external forces.

The total current i at any position within the battery can be described by Equation (1).[25]

$$i = \frac{F^2 A}{RT} \cdot \frac{\partial \phi}{\partial x} \sum_j z_j^2 D_j C_j + FA \sum_j z_j D_j \frac{\partial C_j}{\partial x} \quad (1)$$

F is Faraday constant and R is gas constant. For a substance j, A (area), T (absolute temperature), z_j (charge on species j in signed units of electronic charge), and D_j (diffusion coefficient of species j) is invariant. C_j is concentration of species j. The second term in Equation (1) represents the diffusion current, primarily governed by the concentration gradient of ions ($\frac{\partial C_j}{\partial x}$). Therefore, ion transport near the electrode surface is dominated by diffusion, controlled by surface redox reactions. The first term indicates the migration current, which depends on the gradient of electric potential ($\frac{\partial \phi}{\partial x}$), or electric field intensity. Further from the electrode, where the ionic concentration gradients are small, ion transport is driven primarily by migration, influenced by the electric field. Compared to circular electrodes (Figure 4f), fiber electrodes with a rectangular cross-section (Figure 4g) yield a more uniform electric field between electrodes and a higher overall electric field intensity, thus achieving a more uniform current distribution and an increased current. This structural optimization enhances long-term cycling stability and zinc ion transport.

2.4. Electrochemical Performance of the $H_2V_3O_8$@Ni@CF

The electrochemical performance of the $H_2V_3O_8$ fiber electrode was evaluated using a zinc strip as the counter electrode, separated by a glass fiber separator, with electrolyte injected. All components were packaged in a fluorinated ethylene propylene (FEP) membrane and heat-sealed. Electrochemical tests were conducted within a voltage window of 0.2 to 1.6 V. **Figure 5a** presents the cyclic voltammograms (CV) curves of the $H_2V_3O_8$@Ni@CF battery for the first two cycles at a scan rate of 1 mV s^{-1}. The nearly overlapping cycles indicated good reaction reversibility. Multiple reduction and oxidation peaks were observed. The cathodic peaks at 0.39 and 0.87 V corresponded to the intercalation of zinc ions, and the anodic peaks at 0.80 and 1.05 V corresponded to the deintercalation of zinc ions.

Figure 5b compares the cycling stability of rectangular and circular $H_2V_3O_8$@Ni@CF electrodes at a current density of 3 A g^{-1}. The rectangular electrode achieved capacities of 235, 234, and 225 mAh g^{-1} at the 50th, 100th, and 200th cycles, respectively (Figure 5c), demonstrating high capacity and good cycling stability. A pronounced increase in specific capacity was observed in the first 20 cycles, which was attributed to the gradual saturation of the electrode by the electrolyte. The circular fiber electrode was included as a reference. Unlike the rectangular electrode, the circular fiber did not exhibit a significant specific capacity increase, indicating that the rectangular structure was denser and required a longer activation period. The rectangular electrode maintained a higher specific capacity and a more stable cycling profile than the circular electrode, which showed capacity decay after several cycles. These results highlight the advantages of the pressing process and the rectangular electrode design, as the denser structure effectively retards capacity loss during cycling.

Subsequent electrochemical characterization focused on the rectangular fiber electrode. Figure 5d presents the rate performance of $H_2V_3O_8$@Ni@CF at various current densities. The discharge specific capacities were 410, 308, 269, 212, 122, and 66 mAh g^{-1} at current densities of 0.1, 0.5, 1, 2, 5, and 10 A g^{-1}, respectively (Figure 5e). Upon returning the current density to 0.1 A g^{-1}, the electrode delivered a specific discharge capacity of 361 mAh g^{-1}, demonstrating robust rate capability. The Nyquist plot (Figure S6, Supporting Information) confirmed that the fiber battery exhibited low series resistance (R_s) and charge transfer resistance (R_{ct}), indicating efficient electron and ion transport during operation.

The CV curves at different scan rates (Figure 5f) further revealed the reaction kinetics of the fiber electrode and the advantages of $H_2V_3O_8$ as the active material. Analysis of the relationship between peak current and scan rate (Figure S7a–c, Supporting Information) showed that the charge storage was dominated by a surface-controlled process, rather than diffusion. The high capacitive contribution indicates rapid reaction kinetics, resulting in excellent rate performance. This feature also stabilizes the $H_2V_3O_8$ structure, mitigates volume expansion, and yields stable cycling.[26]

The zinc-ion storage mechanism of $H_2V_3O_8$@Ni@CF during charge/discharge was investigated by ex situ XRD and XPS. The ex situ XRD patterns (Figure 5g,h) captured structural evolution at various charge/discharge states. The pristine spectrum displayed characteristic peaks of $H_2V_3O_8$. Upon discharge to 0.6 V, new diffraction peaks emerged. Full discharge to 0.2 V led to the intensification of peaks at 12.3°, 30.1°, and 36.5°, indicating the formation of a new phase. During charging from 0.2 to 1.0 V, these peaks weakened and eventually disappeared after full

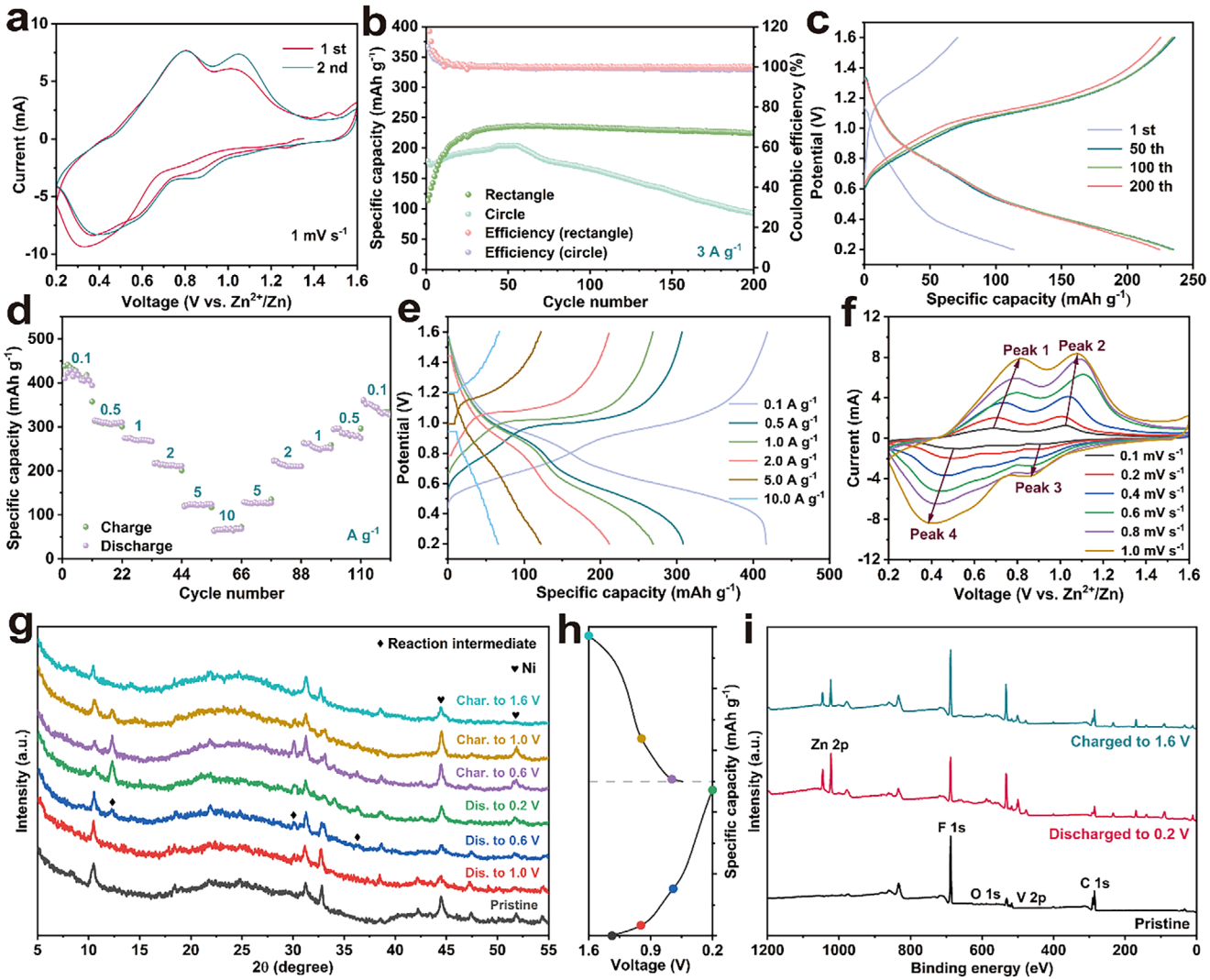

Figure 5. Electrochemical performance and zinc-storage mechanism analysis of $H_2V_3O_8$@Ni@CF. a) CV curves at 1 mV s^{-1}. b) Cycling stability of rectangular and circular $H_2V_3O_8$@Ni@CF at 3 A g^{-1}. c) Galvanostatic charge–discharge(GCD) profiles of rectangular $H_2V_3O_8$@Ni@CF at 3 A g^{-1}. d) Rate capability of rectangular $H_2V_3O_8$@Ni@CF. e) GCD profiles at different current densities. f) CV curves at scan rates from 0.1 to 1.0 mV s^{-1}. g) Ex situ XRD patterns at different charge/discharge states. h) Corresponding GCD curves after 5 cycles. i) XPS spectra after 5 cycles.

charge, confirming the reversibility of the reaction. Additionally, the (200) peak shifted from 10.44° to 10.65° during discharge, reflecting a decrease in layer spacing due to the strong electrostatic attraction between Zn^{2+} and the two negatively charged V_3O_8 layers.[6,27,28] As the electrode was charged to 1.6 V, the (200) peak returned to its original position, further supporting the high reversibility of Zn^{2+} insertion/extraction.

XPS spectra (Figure 5i) at different charge/discharge states were used to examine valence changes during cycling. After discharge to 0.2 V, two strong peaks at 1022.7 and 1045.8 eV appeared in the Zn 2p region, indicating Zn^{2+} intercalation. The intensity of these peaks was higher at full discharge than at full charge, confirming Zn^{2+} extraction from the cathode during charging (Figure S8a, Supporting Information). High-resolution V 2p XPS spectra (Figure S8b, Supporting Information) showed peaks at 516.0 and 517.5 eV, corresponding to V^{4+} and V^{5+}, respectively. After full discharge, the V^{4+}/V^{5+} ratio increased, indicating reduction from V^{5+} to V^{4+}. After charging, the valence state returned to the initial condition, confirming the reversibility of the redox process. XPS spectra after 50 cycles (Figure S9, Supporting Information) were similar to those after 5 cycles, demonstrating good long-term cycling stability. Surface SEM images (Figures S10 and S11, Supporting Information) of $H_2V_3O_8$@Ni@CF after 50 cycles revealed preserved structural integrity. EDX mappings at 1.6 and 0.2 V confirmed Zn^{2+} extraction/insertion during charge/discharge.

2.5. Mechanical Performance of the $H_2V_3O_8$@Ni@CF

The preceding tests established the good electrochemical performance of $H_2V_3O_8$@Ni@CF fiber electrodes. A standard tensile test was performed on $H_2V_3O_8$@Ni@CF, with the 1k Ni@CF also tested for comparison. **Figure** 6a presents the

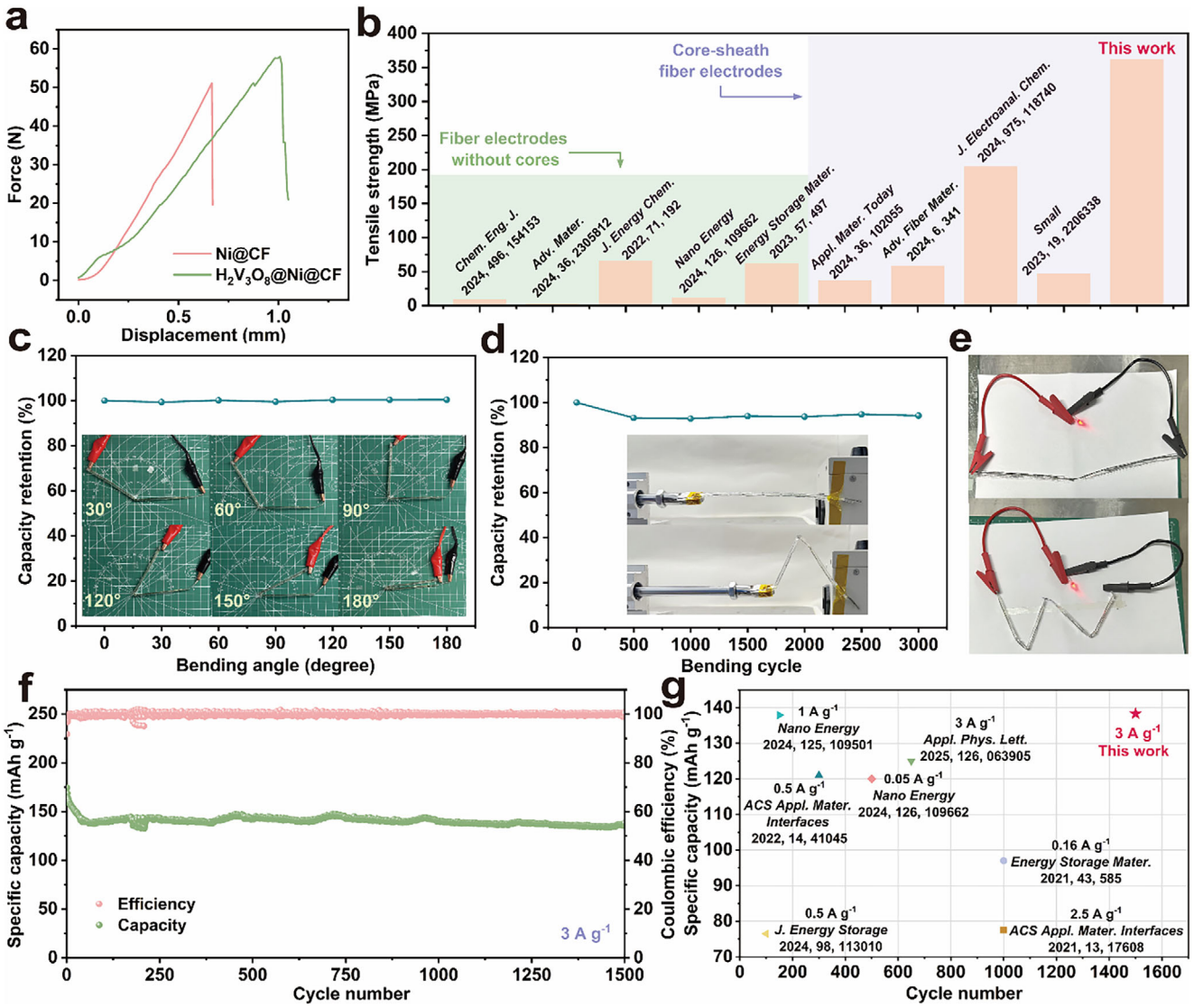

Figure 6. Mechanical performance of $H_2V_3O_8$@Ni@CF and electrochemical performance of $H_2V_3O_8$@Ni@CF//Zn@Ni@CF fiber battery. a) Force–displacement curves of $H_2V_3O_8$@Ni@CF and Ni@CF. b) Ultimate tensile strength of various fiber electrodes. c,d) Capacity retention at 3 A g^{-1} at different c) bending angles and d) bending cycles. e) Photographs of an LED powered by two straight (top) and bent (bottom) fiber batteries. f) Cycling stability of $H_2V_3O_8$@Ni@CF//Zn@Ni@CF fiber battery at 3 A g^{-1}. g) Specific capacity versus cycle number for different fiber batteries.

force–displacement curves for both fibers. The ultimate tensile strength of $H_2V_3O_8$@Ni@CF was 361.9 MPa, while Ni@CF exhibited 922.6 MPa. The similar maximum force for both fibers indicates that the presence of the active material does not significantly compromise the mechanical properties of the composite structure. The decrease in ultimate tensile strength is primarily attributed to the increase in cross-sectional area due to the coating, in agreement with the mechanical behavior of composite materials.

Figure 6b compares the ultimate tensile strengths of fiber electrodes reported in previous studies.[2,29–36] Core–sheath fiber electrodes generally show superior mechanical properties. Fiber electrodes without cores are formed by directly mixing the active material, conductive agent, and binder, with organic polymers providing mechanical support. This results in relatively low tensile strength, which limits processability and suitability for load-bearing applications. Owing to the use of CF as the core, $H_2V_3O_8$@Ni@CF achieves higher tensile strength than most previously reported fiber electrodes.

2.6. The CF Current Collector Battery

In the above tests, zinc strips were used as anodes with aqueous electrolyte to assess the electrochemical performance of the fiber cathodes and minimize external interference. However, zinc, as a metal, lacks the mechanical flexibility of fiber cathodes with CF cores. For example, zinc strips cannot bend freely in multiple directions, limiting the flexibility of the assembled fiber battery. To meet structural energy storage requirements, a flexible

fiber anode based on CF is needed. Benefiting from the electrical conductivity of Ni@CF, a zinc fiber anode (Zn@Ni@CF) was prepared via electrochemical deposition. In addition, a PAM hydrogel electrolyte replaced the aqueous electrolyte to enhance flexibility and prevent severe liquid leakage in the event of battery damage.

Figure 6c demonstrates the electrochemical performance of the fiber battery at different bending angles. Bending and subsequent recovery to the original shape did not affect battery performance. The nearly identical galvanostatic charge–discharge (GCD) profiles at different bending angles (Figure S12, Supporting Information) supported this conclusion. The fiber battery was subjected to repeated bending (Figure 6d). Capacity retention declined slightly after 500 cycles, then stabilized. After 3000 bending cycles, the battery retained 94% of its initial capacity, as shown by the GCD profiles in Figure S13 (Supporting Information). Two fiber batteries in series could power an LED, maintaining function even under bending (Figure 6e).

Figure 6f shows the cycling performance of the CF current collector battery. The device displayed a long cycle life of 1500 cycles at a current density of 3 A g^{-1}, with a specific capacity of 138 mAh g^{-1} at the final cycle and a Coulombic efficiency consistently above 95%. An initial decline in specific capacity was noted during the first 35 cycles, and the final capacity was lower than that observed in electrode-level tests. Two main factors contributed to this: First, Zn@Ni@CF served as the anode instead of a zinc strip. Although pressed to approximate the geometry of a zinc strip, Zn@Ni@CF inherently possesses a more complex surface, which introduces interfacial complexity. Additionally, zinc tends to form dead zinc during cycling, further contributing to capacity loss. Second, hydrogel electrolytes generally penetrate the fiber electrode less efficiently than liquid electrolytes. To minimize prolonged activation time, the electrodes were presoaked in aqueous electrolyte before assembly, potentially resulting in higher water content. This could gradually dissolve some vanadium oxide from the fiber, causing active material loss and reduced specific capacity. Despite these challenges, the fiber electrode in this study exhibited advantages in specific capacity and cycling life when compared to reported devices (Figure 6g, with detailed data in Table S1, Supporting Information).[36–42] Rate performance tests of the CF current collector battery (Figure S14, Supporting Information) revealed discharge specific capacities of 186, 140, 112, and 93 mAh g^{-1} at current densities of 2, 3, 4, and 5 A g^{-1}, respectively.

This work highlights the advantages of the high-performance fiber cathode, which enables flexible and robust batteries. $H_2V_3O_8$@Ni@CF achieved an energy density of 131 Wh kg^{-1} at a power density of 1.65 kW kg^{-1}, based on the active mass of the cathode in electrode-level tests. The fiber electrode also demonstrated promising energy storage in comparison with similar reports (Table S1, Supporting Information). When considering the total mass of the full battery (cathode, electrolyte, anode, and encapsulation), the energy density was 5.0 Wh kg^{-1} at a power density of 0.05 kW kg^{-1}. This reduction is mainly due to the significant mass contribution from the hydrogel electrolyte and encapsulation materials. Thus, optimizing the fiber cathode is only the first step in fiber battery development. The next priorities are: 1) integrating zinc with fiber materials to match the mechanical properties of the cathode and anode; 2) addressing the dendrite formation issue associated with the complex morphology of zinc/CF composite anodes, an issue more severe than for planar zinc strips;[43] and 3) developing quasi-solid-state,[44] and solid-state electrolytes,[45] and novel encapsulation materials to ensure reliable battery operation under deformation and stress.[46,47] These directions represent promising areas for future research.

3. Conclusion

A fiber cathode suitable for zinc-ion fiber batteries was developed using $H_2V_3O_8$ as the active material for its high specific capacity and nickel-plated CF as the core material for their strength, flexibility, and electrical conductivity. The combination of these materials resulted in a fiber electrode with enhanced electrochemical and mechanical performance. A pressing process, leveraging the shape deformability of CF, was employed to optimize the fiber shape, which increased the specific capacity and maintained long-cycle stability. In the preparation process, efficiency and universality were prioritized. A wet-spinning method enabled the continuous, simple, and cost-effective fabrication of fibers, supporting large-scale production. The $H_2V_3O_8$@Ni@CF fiber cathode achieved an ultimate tensile strength of 361.9 MPa and a specific capacity of 225 mAh g^{-1} at 3 A g^{-1}. When assembled with a Zn@Ni@CF fiber anode and PAM hydrogel electrolyte into a CF current collector fiber battery, it demonstrated satisfactory flexibility and shape conformability. At a current density of 3 A g^{-1}, the battery maintained a specific capacity of 138 mAh g^{-1} after 1500 cycles, demonstrating favorable electrochemical performance. This work presents a strategy integrating structure design, material synthesis, and process engineering, achieving a balance between electrochemical and mechanical performance by utilizing the properties of CF. The results support the development of flexible electronics and structural energy storage technologies.

4. Experimental Section

Materials: Vanadium pentoxide (V_2O_5, 98%, Sigma–Aldrich), D-glucose monohydrate ($C_6H_{12}O_6{\cdot}H_2O$, 98%, Aladdin), polyvinylidene fluoride (PVDF, analytical reagent, Arkema), acetylene black (Hefei Kejing Material Technology Co., Ltd.), zinc sulfate monohydrate ($ZnSO_4{\cdot}H_2O$, 99.9%, Aladdin), sodium citrate ($C_6H_5Na_3O_7$, 98%, Aladdin), *N*-methyle-2-pyrrolidone (NMP, 99.5%, Aladdin), zinc trifluoromethanesulphonate ($Zn(CF_3SO_3)_2$, 98%, Macklin), nickel-plated CF (1k, Suzhou Xinna New Material Technology Co., Ltd.), zinc strips (0.05 mm thick, Hefei Shushan Wenghou Metal Material Co.), acrylamide (AM, 99%, Aladdin), *N,N'*-Methylenebisacrylamide (MBAA, AR, Macklin), and ammonium persulfate ($(NH_4)_2S_2O_8$, 98%, Shanghai Lingfeng Chemical Reagents Co., Ltd.).

Preparation of the $H_2V_3O_8$ Fiber Electrodes ($H_2V_3O_8$@Ni@CF): To prepare the $H_2V_3O_8$ nanowires, 0.436 g of V_2O_5 and 12 mL of deionized water were first placed in one side of a Teflon-lined multichambered autoclave. In the other side of the autoclave, 0.048 g $C_6H_{12}O_6{\cdot}H_2O$ and 12 mL of deionized water were added. When the reaction solution was heated to 240 °C, the rotating Teflon-lined multichambered autoclave started to mix the two sides of the solution, and the reaction was continued for 1 h. The product was collected by vacuum filtration. The green powder sample was obtained after vacuum drying at 80 °C for 24 h.

For the fabrication of $H_2V_3O_8$@Ni@CF, $H_2V_3O_8$ (70 wt.%) and acetylene black (10 wt.%) were thoroughly ground, and then mixed with PVDF (20 wt.%) to form a uniform slurry in NMP. The resulting slurry (250 mg

mL^{-1}) was loaded into a syringe barrel for wet spinning. This syringe barrel was fitted to a special tapered concave nozzle with coaxial dual channels. The Ni@CF passed through the inner channel, while the slurry was extruded through the outer channel. The extruded slurry entered a coagulation bath (water) at a speed of 23 mm s^{-1}. After a solvent exchange in the coagulation bath, stable fibers formed. These fibers were pulled, dried, and then pulled again to change the cross-section initially. Afterward, the fiber electrodes were pressed between two plates to yield a rectangular cross-section. The effective mass loading of the active material was 1.31 mg cm^{-1}.

Characterization: Morphologies and elemental distributions were characterized by field emission scanning electron microscopy (FE-SEM, Quanta FEG 250) equipped with EDX. The crystal structures were identified by XRD (Empyrean) using Cu Kα radiation ($\lambda = 1.5406$ Å) at 45 kV and 40 mA. Raman spectroscopy (Invia Microscope, Renishaw) with a 532 nm laser source and XPS (AXIS-Ultra DLD) were used to analyze surface chemical compositions. Mechanical tensile tests were conducted using a universal testing machine (Instron 3343). The ultimate tensile strength σ was calculated with the equation: $\sigma = \frac{F_{max}}{A}$, where F_{max} is the maximum load measured in the tensile test, and A is the cross-sectional area of the tested fiber.

Battery Assembly and Electrochemical Characterization: For electrochemical tests, the $H_2V_3O_8$@Ni@CF was separated from a zinc strip by a glass microfiber filter membrane (0.675 mm thick, Whatman GF/D). All components were sealed in a FEP membrane. Portions of the Ni@CF and zinc strip were left exposed as current collectors. The electrolyte (3 M $Zn(CF_3SO_3)_2$ aqueous solution) was then injected, and the battery was heated to seal it.

For the fiber battery, the $H_2V_3O_8$@Ni@CF and Zn@Ni@CF were separated by the PAM hydrogel electrolyte and encapsulated in a FEP membrane. (Preparation details for Zn@Ni@CF and the PAM hydrogel electrolyte are provided in the Supporting Information.)

A multichannel battery testing system (Land CT2001A) and an electrochemical workstation (CHI660E) were used for electrochemical measurements. GCD performance and CV curves were recorded in the potential range of 0.2 to 1.6 V. Electrochemical impedance spectroscopy (EIS) was measured across a frequency range from 10^6 to 10^{-1} Hz with a 5 mV amplitude. All measurements were conducted at room temperature (25 °C).

Supporting Information

Supporting Information is available from the Wiley Online Library or from the author.

Acknowledgements

J.X. and Z.Z. contributed equally to this work. This work was supported by the National Natural Science Foundation of China (No. 52372200, 52171203, and 52371214) and the Frontier Technologies R&D Program of Jiangsu (Grant no. BF2024033).

Conflict of Interest

The authors declare no conflict of interest.

Data Availability Statement

The data that support the findings of this study are available from the corresponding author upon reasonable request.

Keywords

electrochemical performance, $H_2V_3O_8$, mechanical strength, structural design, wet spinning, zinc-ion fiber battery

Received: April 23, 2025
Revised: June 23, 2025
Published online:

[1] W. Cheng, L. Sun, J. Dong, Z. Han, L. Wei, L. Lu, R. Sun, *Energy Storage Mater.* **2025**, *75*, 104059.
[2] J. Pu, Q. Cao, Y. Gao, Q. Wang, Z. Geng, L. Cao, F. Bu, N. Yang, C. Guan, *Adv. Mater.* **2024**, *36*, 2305812.
[3] S. Xu, P. Shen, Z. Shen, R. Chen, D. Zhang, Z. Zhao, Y. Zhang, D. Li, Y. Xiong, X. Wang, Y. Hu, J. Zhao, *Chem. Eng. J.* **2025**, *504*, 158509.
[4] X. Wang, P. Lei, C. Zheng, Z. Wang, B. Wang, X. Cui, J. Cheng, *Adv. Funct. Mater.* **2025**, 2500916.
[5] P. Hu, P. Hu, T. D. Vu, M. Li, S. Wang, Y. Ke, X. Zeng, L. Mai, Y. Long, *Chem. Rev.* **2023**, *123*, 4353.
[6] P. He, Y. Quan, X. Xu, M. Yan, W. Yang, Q. An, L. He, L. Mai, *Small* **2017**, *13*, 1702551.
[7] Q. An, J. Sheng, X. Xu, Q. Wei, Y. Zhu, C. Han, C. Niu, L. Mai, *New J. Chem.* **2014**, *38*, 2075.
[8] M. Rastgoo-Deylami, M. S. Chae, S. T. Hong, *Chem. Mater.* **2018**, *30*, 7464.
[9] J. He, C. Lu, H. Jiang, F. Han, X. Shi, J. Wu, L. Wang, T. Chen, J. Wang, Y. Zhang, H. Yang, G. Zhang, X. Sun, B. Wang, P. Chen, Y. Wang, Y. Xia, H. Peng, *Nature* **2021**, *597*, 57.
[10] C. Lu, H. Jiang, X. Cheng, J. He, Y. Long, Y. Chang, X. Gong, K. Zhang, J. Li, Z. Zhu, J. Wu, J. Wang, Y. Zheng, X. Shi, L. Ye, M. Liao, X. Sun, B. Wang, P. Chen, Y. Wang, H. Peng, *Nature* **2024**, *629*, 86.
[11] I. Marriam, M. Tebyetekerwa, H. A. Memon, H. Chathuranga, J. Yang, K. Sun, D. Chu, C. Yan, *Adv. Mater. Technol.* **2025**, *10*, 2400753.
[12] H. Yi, Y. Ma, S. Zhang, B. Na, R. Zeng, Y. Zhang, C. Lin, *ACS Sustainable Chem. Eng.* **2019**, *7*, 18894.
[13] Y. Li, Q. Guan, J. Cheng, B. Wang, *Energy Storage Mater.* **2022**, *49*, 227.
[14] X. Cheng, X. Yang, Y. Zhang, P. Lv, J. Yang, F. Huang, Q. Wei, *Adv. Fiber Mater.* **2023**, *5*, 650.
[15] L. Chen, K. Hu, K. Yang, M. Yanilmaz, X. Han, Y. Liu, X. Zhang, *Carbon* **2023**, *215*, 118461.
[16] X. Lan, T. Tang, H. Xie, S. W. Hasan, L. Liang, Z. Q. Tian, P. K. Shen, *Nano Lett.* **2022**, *22*, 5795.
[17] B. Dai, X. Shi, X. Pei, F. Xu, Y. Zhao, *Energy Storage Mater.* **2024**, *66*, 103231.
[18] M. Li, Z. Li, X. Ye, W. He, L. Qu, M. Tian, *Adv. Funct. Mater.* **2023**, *33*, 2210111.
[19] M. Li, Z. Li, X. Ye, X. Zhang, L. Qu, M. Tian, *ACS Appl. Mater. Interfaces* **2021**, *13*, 17110.
[20] J. Yang, H. Tian, Y. Li, H. Li, S. Li, H. Yang, M. Ding, X. Wang, P.-Y. Chen, *Energy Storage Mater.* **2022**, *53*, 352.
[21] P. Liang, T. Xu, K. Zhu, Y. Rao, H. Zheng, M. Wu, J. Chen, J. Liu, K. Yan, J. Wang, R. Zhang, *Energy Storage Mater.* **2022**, *50*, 63.
[22] S. Tan, Y. Jiang, Q. Wei, Q. Huang, Y. Dai, F. Xiong, Q. Li, Q. An, X. Xu, Z. Zhu, X. Bai, L. Mai, *Adv. Mater.* **2018**, *30*, 1707122.
[23] T. Hu, Y. Liu, Y. Zhang, M. Chen, J. Zheng, J. Tang, C. Meng, *J. Colloid Interface Sci.* **2018**, *531*, 382.
[24] T. Khudiyev, B. Grena, G. Loke, C. Hou, H. Jang, J. Lee, G. H. Noel, J. Alain, J. Joannopoulos, K. Xu, J. Li, Y. Fink, J. T. Lee, *Mater. Today* **2022**, *52*, 80.
[25] A. J. Bard, L. R. Faulkner, *Electrochemical Methods, Fundamentals and Applications*, 2nd ed., Wiley, New York **2001**.
[26] B. Cong, Y. Hu, S. Sun, Y. Wang, B. Wang, H. Kong, G. Chen, *Nanoscale* **2020**, *12*, 16901.
[27] C. Liu, W. Xu, C. Mei, M. Li, X. Xu, Q. Wu, *Chem. Eng. J.* **2021**, *405*, 126737.
[28] Q. Pang, C. Sun, Y. Yu, K. Zhao, Z. Zhang, P. M. Voyles, G. Chen, Y. Wei, X. Wang, *Adv. Energy Mater.* **2018**, *8*, 1800144.

[29] Y. Tang, M. Li, Y. Liu, X. Guo, Y. Liu, C. Wang, Y. Li, M. Tian, *Appl. Mater. Today* **2024**, *36*, 102055.
[30] T. Gao, G. Yan, X. Yang, Q. Yan, Y. Tian, J. Song, F. Li, X. Wang, J. Yu, Y. Li, S. Guo, *J. Energy Chem.* **2022**, *71*, 192.
[31] H. Wang, Y. Lu, Z. Nie, H. Liu, B. Dai, X. Shi, B. Yan, T. Zhao, Z. Zhang, J. Zhu, Y. Zhao, *Small* **2023**, *19*, 2206338.
[32] X. Ma, H. Zhang, Y. Liu, W. Yan, C. Chen, K. Zhang, *J. Electroanal. Chem.* **2024**, *975*, 118740.
[33] C. Zhao, R. Wang, H. Liang, B. Fang, R. Li, R. Wu, R. Mo, *Chem. Eng. J.* **2024**, *496*, 154153.
[34] Y. Li, Y. Wang, Y. Liu, Z. Lin, Z. Ye, J. Wang, J. Qiu, H. Zhang, G. Cao, *Energy Storage Mater.* **2023**, *57*, 497.
[35] I. Marriam, M. Tebyetekerwa, H. Chathuranga, K. Sun, A. Du, C. Yan, *Adv. Fiber Mater.* **2024**, *6*, 341.
[36] L. Li, Y. Chen, S. Wang, D. Pei, M. Li, T. Li, C. Li, *Nano Energy* **2024**, *126*, 109662.
[37] Z. Cong, W. Guo, P. Zhang, W. Sha, Z. Guo, C. Chang, F. Xu, X. Gang, W. Hu, X. Pu, *ACS Appl. Mater. Interfaces* **2021**, *13*, 17608.
[38] N. Wang, S. Zhai, Y. Ma, X. Tan, K. Jiang, W. Zhong, W. Zhang, N. Chen, W. Chen, S. Li, G. Han, Z. Li, *Energy Storage Mater.* **2021**, *43*, 585.
[39] H. Zhang, T. Xiong, T. Zhou, X. Zhang, Y. Wang, X. Zhou, L. Wei, *ACS Appl. Mater. Interfaces* **2022**, *14*, 41045.
[40] Z. Jiang, Y. Wang, H. Chen, S. Zhai, M. Li, P. Songsiriritthigul, T. Z. Oo, N. W. Lwin, M. Zaw, K. S. Hui, F. Chen, *J. Energy Storage* **2024**, *98*, 113010.
[41] X. Cheng, H. Gao, X. Tian, D. Wu, P. Lv, S. S. Yoon, J. Yang, Q. Wei, *Nano Energy* **2024**, *125*, 109501.
[42] H. Lei, X. Zhou, Z. Chen, Y. Liang, D. Qiu, X. Yang, Z. Wang, W. Mai, *Appl. Phys. Lett.* **2025**, *126*, 063905.
[43] H. Wang, Y. Liu, M. Zhu, Y. Chen, D. Chen, Z. Lin, K. Wang, Z. Xu, S. Chen, G. Xing, O. I. Malyi, Y. Tang, Y. Zhang, *Angew. Chem., Int. Ed.* **2025**, *64*, 202414473.
[44] Y. Chen, M. Zhu, C. Li, H. Wang, D. Chen, H. Wu, Z. Huang, Y. Wang, Y. Fan, Z. Bai, S. Chen, Y. Tang, Y. Zhang, *Adv. Funct. Mater.* **2025**, 2501162.
[45] M. Zhu, H. Wang, H. Wang, C. Li, D. Chen, K. Wang, Z. Bai, S. Chen, Y. Zhang, Y. Tang, *Angew. Chem., Int. Ed.* **2024**, *63*, 202316904.
[46] X. Gong, H. Jiang, C. Lu, K. Zhang, Y. Long, Z. Yang, S. Sun, Y. Chang, L. Ma, H. Peng, B. Wang, *Adv. Mater.* **2024**, *36*, 2409910.
[47] H. Jiang, X. Gong, J. Wang, Z. Yang, C. Li, Y. Long, C. Lu, S. Sun, K. Zhang, Y. Chang, P. Li, X. Cheng, H. Peng, B. Wang, *Adv. Funct. Mater.* **2024**, *34*, 2408529.